*J. Fluid Mech.* (2026), *vol.* 1026, R1, doi:10.1017/jfm.2025.11000



# Harnessing cilium oscillations for enhanced transport in chaotic flow

**Chao-Ben Zhao**[1,2], **Kai Leong Chong**[1], **Chao Sun**[2,3] and **Quan Zhou**[1]

[1]Shanghai key Laboratory of Mechanics in Energy Engineering, Shanghai Institute of Applied Mathematics and Mechanics, School of Mechanics and Engineering Science, Shanghai University, Shanghai 200072, PR China

[2]New Cornerstone Science Laboratory, Center for Combustion Energy, Key Laboratory for Thermal Science and Power Engineering of Ministry of Education, Department of Energy and Power Engineering, Tsinghua University, Beijing 100084, PR China

[3]Department of Engineering Mechanics, School of Aerospace Engineering, Tsinghua University, Beijing 100084, PR China

**Corresponding author:** Kai Leong Chong, klchong@shu.edu.cn

(Received 1 October 2025; revised 27 November 2025; accepted 27 November 2025)

We present a novel approach to harness the oscillation energy from cilia in chaotic flow to enhance scalar transport, addressing limitations of the laminar boundary layer. In contrast to the scallop theorem, where reciprocal motion yields negligible transport, coordinated rigid cilium oscillations in chaotic flow trigger boundary-layer resonance, significantly boosting scalar transport at specific frequencies. Under relatively high rigidity, the cilia undergo only small elastic deformations at the driving frequency, and their strokes remain nearly time symmetric. Nevertheless, unlike the classical expectation that reciprocal motion yields negligible transport, coordinated rigid cilium oscillations in chaotic flow trigger boundary-layer resonance, producing a sharp, frequency-selective boost in transport. At low to medium frequencies, cilium-driven fluid displacement enhances transport via vertical mixing. Above a critical frequency, rapid cilium motion induces unstable shear flow, generating coherent vortical structures that amplify mixing in chaotic flow regimes. These vortices, which interact with the inherent coherent structures of the chaotic flow, dramatically improve the efficiency of transport. Our findings reveal a dynamic coupling between cilium-driven resonance and chaotic flow coherent structures, providing a paradigm for optimising transport in thermal systems through active flow control.

**Key words:** convection, buoyancy-driven instability

© The Author(s), 2025. Published by Cambridge University Press.



https://doi.org/10.1017/jfm.2025.11000 Published online by Cambridge University Press

## 1. Introduction

Ciliate-like structures are abundant in nature, manifesting in various forms such as the cilia found on plant leaves, paramecia, coral surface structures (Eloy & Lauga 2012; Shapiro *et al.* 2014; Bouhouche *et al.* 2022), as well as in the respiratory system and oviducts (Koyama, Shi & Fujimori 2019; Causa *et al.* 2025). These structures interact with the surrounding fluid, impacting the morphology of the flow field and playing crucial roles in diverse biological activities (Brennen & Winet 1977; Kim *et al.* 2003; Liu, Powers & Breuer 2011, 2025*a*,*b*). For instance, the active oscillation of sperm cilia effectively aids in their own movement (Gaffney *et al.* 2011; Lauga & Goldstein 2012). Furthermore, the oscillating cilia found on paramecia and coral surfaces generate vortices, enabling the exchange of nutrients and gases with the environment in a captivating display of fluid dynamics. Behind these phenomena, the collective role of cilia plays an important role in the life activities of these organisms. Cilia, found in diverse biological structures like the respiratory system and oviducts, employ coordinated oscillations to achieve tasks as varied as dust and egg transportation, fluid mixing and nutrient exchange, often characterised as metachronal waves (Gilpin, Bull & Prakash 2020; Mesdjian *et al.* 2022; von Kenne *et al.* 2025).

By harnessing the power of metachronal waves in artificial cilium systems (Coq *et al.* 2011; Elgeti & Gompper 2013; Dong *et al.* 2020; Gu *et al.* 2020), one can observe remarkable potential to enhance material transport and fluid dynamics. Similarly, paramecia and ciliated structures on coral surfaces transport oxygen and nutrients by generating vortices (Shapiro *et al.* 2014; Bouhouche *et al.* 2022). Studies reveal that longitudinal waves maximise mucus transport, while transverse waves minimise energy dissipation by cilia (Mesdjian *et al.* 2022). An important theoretical framework for ciliary dynamics is the scallop theorem (Purcell 1977; Lauga 2011*b*), which asserts that reciprocal motion of rigid bodies in low Reynolds number flows, such as cilia, cannot generate net fluid transport due to the time-reversible nature of the flow (Qiu *et al.* 2014; Esparza López & Lauga 2023). As a result, ciliary systems rely on asymmetric flapping motions, like metachronal waves, to efficiently drive or pump fluid (Hall & Clarke 2020; Kobayashi & Yamamoto 2024; Xia *et al.* 2024). Nevertheless, many cilia operate within chaotic background flows, particularly in artificial cilium systems at relatively larger scales. These chaotic flows introduce additional complexities that challenge traditional models of the ciliary dynamics. For example, enhanced diffusion can be seen for a swimmer in a fluctuating environment (Lauga 2011*a*). However, the precise coupling between cilium carpet and chaotic flows remains poorly understood, and how cilia strategically harness oscillation energy to modify flow structures for enhanced transport efficiency is still unknown, where there is a modified interaction between the flexible structure and the flow (Médéric & Mahadevan 2005; Shelley & Zhang 2011; Alben 2015; Guttag & Reis 2017; Ganedi *et al.* 2018; Mathai *et al.* 2023). Recent progress on flexible fibres in turbulence – reviewed in Marchioli, Rosti & Verhille (2025) – highlights how flexibility enables local coupling with multiscale flow structures. In this context, Mathai *et al.* (2022) demonstrated that a compliant membrane hydrofoil passively cambered, stabilised leading-edge vortices, and achieved up to 160 % higher power than rigid foils. Building on this, Upfal *et al.* (2025) identified constant- and dynamic-camber regimes in which elasticity and extensibility stabilise vortices and soften stall. These insights provide a concise framework for interpreting elastic filament–flow interactions in chaotic convection.

Strikingly, here, we address the open question of how cilium-synchronised oscillation can be utilised in the chaotic flow to optimise scalar transport using thermal systems as an example. Traditionally, the laminar boundary layer imposes a limitation on scalar



https://doi.org/10.1017/jfm.2025.11000 Published online by Cambridge University Press

transport; however, we demonstrate that oscillating cilia can induce resonance within the boundary layer, which enhances transport at intermediate frequencies. Our results demonstrate a mechanistic transition: at low to medium frequencies, cilia uplift fluid, augmenting heat transfer through vertical displacement. Beyond a critical frequency, an intensified flow dynamics generates vortices from unstable shear layers, drastically improving fluid mixing and thermal efficiency. Our findings demonstrate how cilia can exploit chaotic background flows to enhance scalar transport.

To systematically investigate these effects, we consider a paradigm of buoyancy-driven flow – Rayleigh–Bénard (RB) convection, i.e. convective flow inside a cubic box heated from below and cooled from above (Siggia 1994; Ahlers, Grossmann & Lohse 2009; Lohse & Xia 2010; Chillà & Schumacher 2012; Shishkina 2021; Lohse & Shishkina 2023, 2024; Xia *et al.* 2025). Previous studies have explored various strategies to regulate heat transport in thermal convection (Wang *et al.* 2019, 2020; Jiang *et al.* 2020, 2022; Xia *et al.* 2023; Xu *et al.* 2025). Motivated by this, we introduce cilia uniformly distributed on the hot plate, with spacing $\Lambda$ and length $\mathcal{L}$ comparable to the thermal boundary-layer thickness (see figure 1*a*). In this work, we use 'cilia' as a shorthand for wall-mounted oscillating filament arrays, encompassing both biological cilia and engineered flexible fibres. The paper is organised as follows: The numerical set-ups are described in § 2, followed by the heat transfer properties, flow structure and underlying mechanism in § 3. The conclusions are presented in § 4.

## 2. Numerical method

In the present study, we consider the flow within a two-dimensional square box and perform direct numerical simulations (DNS) of thermal convection with an oscillating filament array fixed at the bottom plate. The non-dimensional governing equations under the Boussinesq approximation are

$$\boldsymbol{\nabla}\cdot\boldsymbol{u}=0, \tag{2.1}$$

$$\partial_t\boldsymbol{u}+(\boldsymbol{u}\cdot\boldsymbol{\nabla})\boldsymbol{u}=-\boldsymbol{\nabla}p+\sqrt{\frac{Pr}{Ra}}\nabla^2\boldsymbol{u}+\theta\boldsymbol{e}_z+\boldsymbol{f}, \tag{2.2}$$

$$\partial_t\theta+(\boldsymbol{u}\cdot\boldsymbol{\nabla})\theta=\frac{1}{\sqrt{RaPr}}\nabla^2\theta, \tag{2.3}$$

where $t$ is the dimensionless time scaled by the free-fall time $\sqrt{H/(\alpha g\Delta)}$, $\boldsymbol{u}$ is the fluid velocity scaled by the free-fall velocity $\sqrt{\alpha g\Delta H}$ and $\theta$ is the temperature scaled by the imposed temperature difference $\Delta$; $\boldsymbol{e}_z$ is the unit vector along the vertical direction, and $\boldsymbol{f}$ is the feedback force exerted by the filament on the fluid. All length scales are normalised by the cell height $H$. The Rayleigh number $Ra$ and Prandtl number $Pr$ are defined as

$$Ra=\frac{\alpha g\Delta H^3}{\nu\kappa},\qquad Pr=\frac{\nu}{\kappa}, \tag{2.4}$$

where $\alpha$ is the thermal expansion coefficient, $g$ the gravitational acceleration, $\nu$ the kinematic viscosity and $\kappa$ the thermal diffusivity of the fluid. At the boundaries, no-slip velocity conditions are applied at all walls, with constant temperatures $\theta_{top}=0$ and $\theta_{bot}=1$ at the top and bottom plates, respectively. Adiabatic conditions are applied at the sidewalls.

For the filament, we model inextensible filaments represented by Lagrangian nodes. The dynamics of a thin, flexible filament is governed by (2.5) and (2.6) under the inextensibility



https://doi.org/10.1017/jfm.2025.11000 Published online by Cambridge University Press

constraint (Huang, Shin & Sung 2007; Pinelli *et al.* 2017; Banaei, Rosti & Brandt 2020). The dimensionless equations and the inextensibility condition are

$$\frac{\partial^2 \boldsymbol{X}}{\partial t^2} = \frac{\partial^2 \boldsymbol{X}_f}{\partial t^2} + \frac{\partial}{\partial s}\left(T\frac{\partial \boldsymbol{X}}{\partial s}\right) - \frac{\partial^2}{\partial s^2}\left(B\frac{\partial^2 \boldsymbol{X}}{\partial s^2}\right) - \boldsymbol{F_f} + \boldsymbol{F_c}, \tag{2.5}$$

$$\frac{\partial \boldsymbol{X}}{\partial s} \cdot \frac{\partial \boldsymbol{X}}{\partial s} = 1, \tag{2.6}$$

where $\boldsymbol{X}$ is the filament position, $s$ denotes arclength, $\partial \boldsymbol{X}_f/\partial t$ is the fluid velocity at the filament node, $T$ is the dimensionless tension force, $B$ is the dimensionless bending rigidity, $\boldsymbol{F_f}$ is the fluid force on the filament and $\boldsymbol{F_c}$ is the repulsive force between filament nodes to prevent overlap and self-entanglement. These equations, along with the inextensibility condition, are also described in detail by Huang *et al.* (2007) and Banaei *et al.* (2020).

We induce oscillations in the cilia by changing the boundary conditions and investigate how this modulation affects global heat transport in the system. The boundary condition at the root of cilia is given by

$$\frac{\partial \boldsymbol{X}}{\partial s} = \left[\sin\left(\frac{\pi}{2}\sin(2\pi\Omega t)\right), \cos\left(\frac{\pi}{2}\sin(2\pi\Omega t)\right)\right], \tag{2.7}$$

where $\Omega$ is the oscillation frequency. For thermal coupling, we assume rapid heat exchange between each filament and the surrounding fluid; accordingly, the filament temperature equals the local fluid temperature (the filament is locally isothermal).

For the cilium motion and arrangement, we introduce five additional dimensionless control parameters: the dimensionless tension $T = \mathcal{T}/(\rho_f \alpha g \Delta H)$, the dimensionless bending rigidity $B = \mathcal{B}/(\rho_f \alpha g \Delta H^3)$, the dimensionless frequency $\omega = \sqrt{\Omega^2 H/(\alpha g \Delta)}$, the dimensionless length $L = \mathcal{L}/H$ and the dimensionless spacing $\lambda = \Lambda/H$, where $\rho_f$ is the filament linear density (mass per unit length) (Banaei *et al.* 2020), $\mathcal{T}$ is the cilium tension and $\mathcal{B}$ is the cilium bending rigidity. Unless stated otherwise, we assume neutral buoyancy (the filament density matches that of the surrounding bulk fluid) and fix the bending-rigidity parameter at $B = 0.2$.

To solve the governing equations, we use the finite-difference solver AFiD (Verzicco & Orlandi 1996; Ostilla-Monico *et al.* 2015; van der Poel *et al.* 2015) with a high-performance message passing interface. The equations are solved using a multi-scalar second-order finite-difference method coupled with a fractional third-order Runge–Kutta scheme. Fluid–filament coupling is achieved via the immersed boundary method. The volume force exerted by the filaments on the fluid is computed by convolving the singular forces from the Lagrangian nodes onto the Eulerian mesh (Huang *et al.* 2007; Banaei *et al.* 2020). Our code has been used to simulate various single-phase and multiphase turbulent flow problems (Guo *et al.* 2023; Zhao *et al.* 2024). For fibre-dynamics validation, our results agree with Huang *et al.* (2007) (details in Appendix A). We performed DNS of RB convection with cilium oscillations in both two-dimensional and three-dimensional square boxes. We fixed $Ra = 1 \times 10^7$, $Pr = 4.38$ (corresponding to water conditions) and $\lambda = 0.1$. A series of DNS runs is conducted over the parameter ranges $0.05 \leqslant \omega \leqslant 80$ and $0.04 \leqslant L \leqslant 0.06$. For the three-dimensional cases, we set the aspect ratio of the box to 0.15 for width to height, with a length-to-height ratio of 1 : 1. Cilia are arranged with 30 fibres along the $x$-direction, while the distribution in the $y$-direction follows the same spacing as in the two-dimensional cases.



https://doi.org/10.1017/jfm.2025.11000 Published online by Cambridge University Press

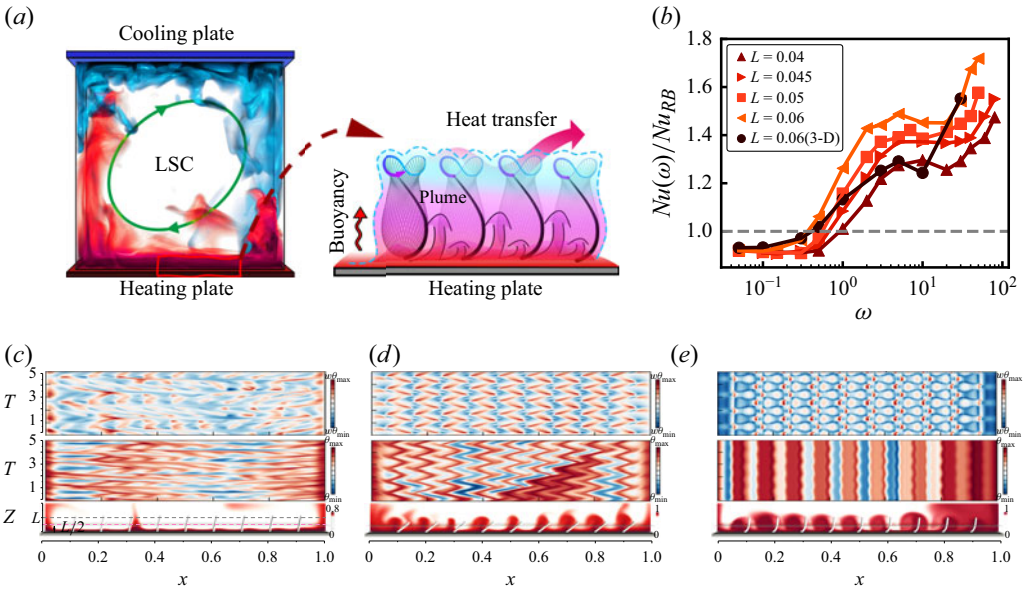



Figure 1. (*a*) Schematic illustrating enhanced heat transport in thermal convection through active cilia, promoting efficient thermal energy redistribution between the heating and cooling plates. (*b*) Normalised Nusselt number $Nu(\omega)/Nu_{RB}$ as a function of oscillation frequency $\omega$ for various cilium lengths $L$ at $Ra = 10^7$ and $Pr = 4.38$. Here, $Nu_{RB}$ denotes the Nusselt number of standard RB convection ($Nu_{RB} = 13.05$ for two dimensions, 16.8 for three dimensions). (*c–e*) Behaviour of plumes within the cilium layer at various oscillation frequencies: $\omega = 0.05$ in (*c*), $\omega = 1$ in (*d*), $\omega = 40$ in (*e*). The middle panels show the vertical slice of temperature at the mid-length of the cilia for each frequency, while the upper panels depict the vertical slice of $w\theta$ at the same location.

## 3. Results

Figure 1(*b*) depicts the variation of the global heat flux $Nu$ with the cilium oscillation frequency $\omega$ at $Ra = 10^7$ and $Pr = 4.38$. It is shown that the dependence of $Nu$ on frequency follows a similar trend, with the $\omega$-dependence of $Nu$ showing three distinct regimes. In the low-frequency range, the $Nu$ value is slightly lower than that of classical RB convection, with oscillating cilia having minimal impact on heat transport. As the frequency $\omega$ increases, the $Nu$ value begins to increase, indicating a substantial enhancement in heat transport due to the oscillating cilia. In particular, in the medium-frequency regime, the $Nu$-trend is not monotonic as $\omega$ increases. A local maximal heat flux is observed, indicating the emergence of a local optimal frequency $\omega_c$ at which the peak value $Nu_c$ is located. Notably, compared with the RB convection, a remarkable $Nu$-enhancement rate reaches up to 50 %. Moreover, we compare the trend of $Nu(\omega)/Nu_{RB}$ for different lengths ($L$) of the cilia. One can see that the onset frequency is sensitive to $L$, and the regime transition shifts toward lower frequencies as the length of the cilia increases.

To gain more insight into the effect of oscillating cilia, we analyse how the flow structures within the ciliary layer are modified by the cilium motions. Figure 1(*c–e*) presents the instantaneous temperature fields within the ciliary layer for frequencies of $\omega = 0.05$ in the low-frequency regime, $\omega = 1$ in the medium-frequency regime and $\omega = 40$ in the high-frequency regime, all at a fixed spacing of $\lambda = 0.1$. In the low-frequency regime (see figure 1*c*), the oscillating cilia have minimal impact on plume emissions (see Supplementary Materials Movie S1 are available at https://doi.org/10.1017/jfm.2025.11000). However, when the frequency exceeds the critical frequency in the medium-frequency regime (see figure 1*d*), the oscillation of



https://doi.org/10.1017/jfm.2025.11000 Published online by Cambridge University Press

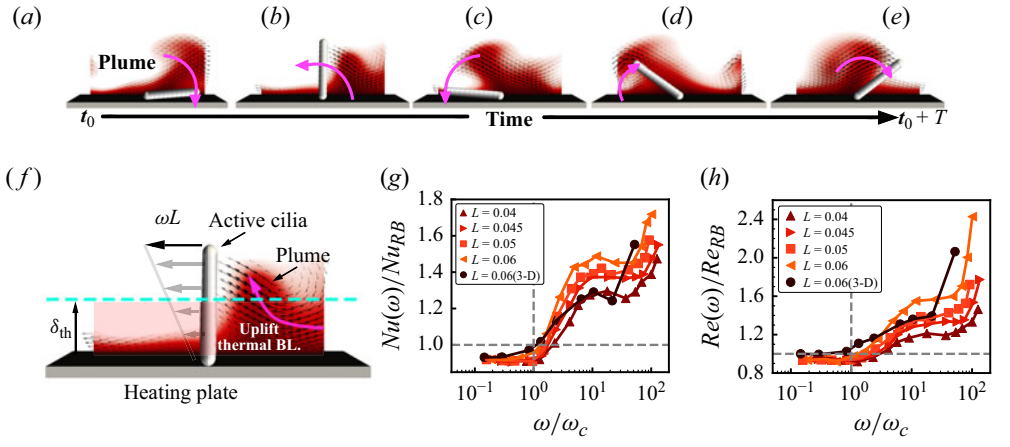



Figure 2. (*a–e*) Morphological evolution of cilia and plumes over one oscillation cycle: active cilia sweep through the temperature field, uplifting the thermal boundary layer and generating plumes. (*f*) Detailed representation of the strong shear effect resulting in a localised uplift mechanism in the thermal boundary layer during the cilia's interactions with the temperature field. (*g*) Normalised Nusselt number $Nu(\omega)/Nu_{RB}$ vs $\omega/\omega_c$ for various cilium lengths $L$. (*h*)Normalised Reynolds number $Re(\omega)/Re_{RB}$ vs $\omega/\omega_c$ for various cilium lengths $L$. The vertical dashed line represents $\omega/\omega_c = 1$ indicates the onset of enhancement in both $Nu$ and $Re$. Here, $Re = \sqrt{\langle u^2 + w^2 \rangle} H/\nu$, with $\langle \cdot \rangle$ denoting spatial and temporal averaging, and $Re_{RB}$ is the Reynolds number for standard RB convection ($Re_{RB} = 184.7$ for two dimensions, 85.7 for three-dimensions).

the cilia disrupts the thermal boundary layer and triggers substantial plume emissions (see Supplementary Materials Movie S2 for details). Under the shear effect of the cilia, the plumes oscillate along with the cilia; as the frequency further increases in the high-frequency regime, the plumes cease to oscillate and instead stabilise with reduced amplitude (see figure 1*e* and Supplementary Materials Movie S3 ). What physics then governs the underlying mechanism of cilium modulation of the plume dynamics?

First, we focus on how oscillating cilia disrupt the thermal boundary layer, thereby triggering significant plume emissions. Figure 2(*a–e*) illustrates the morphological evolution of cilia and plumes over one oscillation cycle: active cilia sweep through the temperature field, uplifting the thermal boundary layer and generating plumes, which suggests a complex interaction between the cilium oscillation and the flow dynamics within the boundary layer (Lee *et al.* 2011; Zhu, He & Zhang 2014; Stein *et al.* 2021). As shown in figure 2(*f*), when cilia sweep through the thermal boundary layer, the shear forces exerted on the surrounding fluid can uplift and destabilise it. Specifically, at low oscillation frequencies, the sweeping time scale $\tau_{os} \sim (\delta_{th}/\omega L)$ exceeds the viscous dissipation time scale $\tau_{dis} \sim (\delta_{th}^2/\nu)$, resulting in rapid dissipation of fluid disturbances without significant disruptions to the flow or temperature fields. In contrast, as the frequency increases and the sweeping time approaches the dissipation time scale, the shear-induced disturbances are not fully dissipated, leading to the continuous acceleration of fluid microstructures. Thus, by balancing these two time scales, we can derive the critical condition $\omega_c \sim (\nu/\delta_{th} L)$. Here, the thermal boundary-layer thickness is obtained from the global Nusselt number as $\delta_{th} = 1/(2Nu)$.

Next, to confirm this proposed physical picture of the onset of $Nu$ enhancement, we replot $Nu(\omega)/Nu_{RB}$ as a function of the normalised frequency $\omega/\omega_c$ for various values of $L$ in figure 2(*g*). The figure shows that the normalised $Nu$ does indeed begin to increase from 1 when $\omega > \omega_c$. This trend is robust across a broad parameter range: additional simulations spanning Rayleigh number $Ra$, filament rigidity $B$ and inter-cilium spacing $\lambda$



https://doi.org/10.1017/jfm.2025.11000 Published online by Cambridge University Press

exhibit the same qualitative dependence of $Nu$ on $\omega/\omega_c$ (see Appendix B). In addition, we present a plot of the normalised Reynolds number $Re(\omega)/Re_{RB}$ versus the oscillation frequency $\omega$ for various cilium lengths $L$ in figure 2(*h*). The qualitative trends indicate that $Re$ exhibits minimal dependence on frequency at low oscillation frequencies, while the Reynolds number remains close to that observed in standard RB convection. However, when the frequency exceeds a critical value, $Re$ increases significantly. Furthermore, the enhancement of $Re$ can also be observed for conditions where $\omega/\omega_c > 1$, reinforcing that our explanation for the onset behaviour is applicable in the $Re$ regime as well (see Appendix B for additional parameters).

It is noteworthy that, during the initial stage of enhancement, the value of $Nu(\omega)/Nu_{RB}$ exhibits a similar trend for different values of $L$. However, with further increases in the ratio $\omega/\omega_c$, a second transition point is observed (see figure 2*g*). For example, at $L = 0.6$ in figure 2(*g*), the normalised $Nu$ begins to rise above 1 when $\omega > \omega_c$. Nevertheless, as the ratio $\omega/\omega_c$ continues to increase (for $\omega/\omega_c > 10$), the normalised $Nu$ starts to level off and even exhibits a slight decrease before increasing again. This behaviour is also reflected in the $Re$ versus $\omega$ relationship shown in figure 2(*h*).

In order to elucidate the transition from the medium-frequency regime to the high-frequency regime (the second transition), we first investigate the influence of ciliary oscillations on heat flux transport within the boundary layer, represented by the parameter $\sqrt{RaPr}\langle w\theta\rangle_L$. As shown in figure 3(*a*), the time series of spatially averaged heat flux $\sqrt{RaPr}\langle w\theta\rangle_L$ within the ciliary layer over five cycles reveals a distinct behaviour: in the medium-frequency regime, characterised by $\omega = 1$, each cycle displays two maxima, while in the high-frequency regime (with $\omega = 40$), only a single maximum is observed. This finding is further confirmed by their corresponding spectral analyses; at $\omega = 1$, the dominant frequency is $f = 2\omega$, while at $\omega = 40$, it is $f = \omega$ (see figure 3*c*,*d*). To gain deeper insights into the flow mechanisms associated with these two dominant frequencies, we present the temperature and velocity fields at the peak moments of thermal transport over one cycle, as shown in figure 3(*e*,*f*). At $\omega = 1$, the two peaks correspond to the occurrence of two significant uplift events induced by ciliary oscillations (see figure 3*e*), as evidenced by the temperature profiles in the midheight of the cilia presented in figure 1(*d*). In contrast, at $\omega = 40$, heat transport is predominantly driven by localised vortices induced by high-frequency oscillations, rather than uplift phenomena associated with ciliary motion. The oscillatory behaviour of the cilia facilitates the emergence of shear vortices during the transition between the first and second half-cycles. This effect can be attributed to the stable shear flow established by the cilia during the initial phase of the cycle; the subsequent rapid directional shift in ciliary motion generates opposing shear forces, thereby promoting the development of localised vortices (see figure 3*f*). Ultimately, this observation underscores the transition between uplift-driven and vortex-driven heat transfer mechanisms.

We further investigate whether the transition from uplift-driven to vortex-driven heat transfer mechanisms arises from the increasing dominance of shear flow dynamics within the ciliary layer. Figure 3(*g*) shows the Reynolds number within the ciliary layer, normalised by the shear Reynolds number $Re_l/Re_s$, as a function of frequency $\omega$. The local Reynolds number is $Re_l = \sqrt{\langle u^2 + w^2\rangle_l}H/\nu$, with $\langle\cdot\rangle_l$ denoting averaging over the ciliary region. The flow intensity driven by the cilia is characterised by the shear Reynolds number $Re_s = \omega LH/\nu$. At low frequencies, flow within the ciliary layer is dominated by large-scale circulation (classical RB convection). As frequency increases, shear from ciliary oscillations becomes dominant. Resonance occurs when the shear Reynolds number approaches the local Reynolds number $Re_l$, at $Re_l/Re_s = 1$. From this, we derive the



https://doi.org/10.1017/jfm.2025.11000 Published online by Cambridge University Press

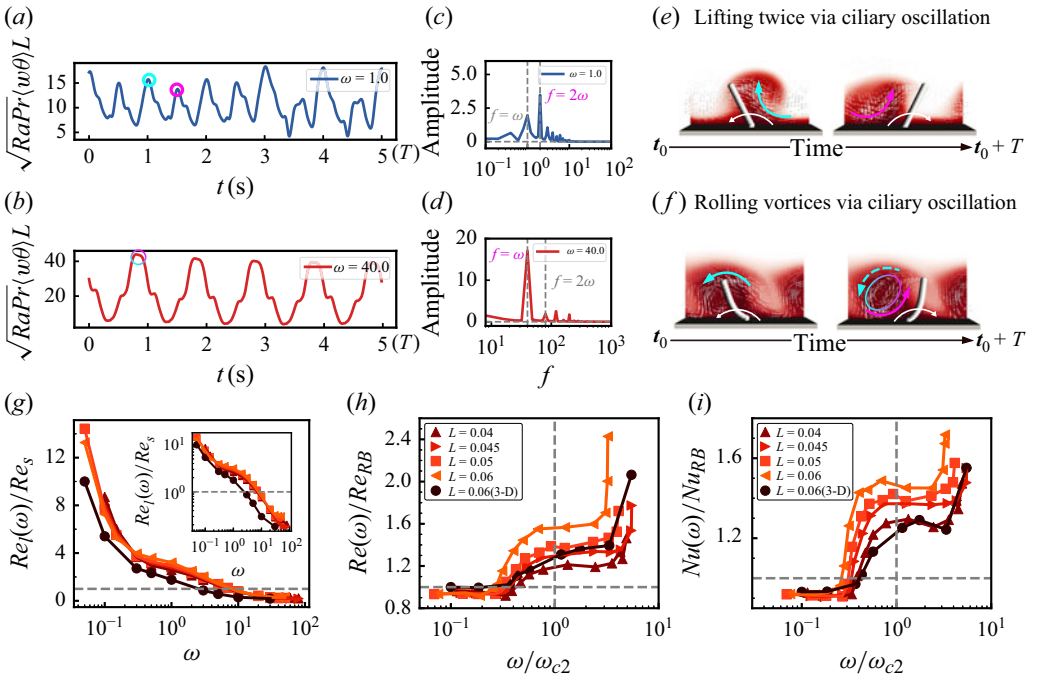



Figure 3. ($a$, $b$) Time series of $\sqrt{RaPr}\langle w\theta\rangle_L$ for different frequencies: $\omega = 1$ ($a$) and $\omega = 40$ ($b$). Here, $\langle\cdot\rangle_L$ denotes averaging over the region within the filament height. Panels ($c$) and ($d$) show the corresponding spectral plots for ($a$) and ($b$), respectively. The black dashed line indicates the proportions at the frequencies $f = \omega$ and $f = 2\omega$. Panels ($e$) and ($f$) present the temperature field (colour) and velocity field (arrows) within the ciliary layer during the cilium oscillation period at moderate frequency ($\omega = 1$) and high frequency ($\omega = 40$). Panel($e$) depicts the event of lifting twice via ciliary oscillation at moderate frequency, while panel($f$) illustrates the event of rolling vortices via ciliary oscillation during the cilium oscillation period at high frequency. ($g$) Normalised Reynolds number $Re_l(\omega)/Re_s$ vs $\omega$ for various cilium lengths $L$. Here, $Re_l = \sqrt{\langle u^2 + w^2\rangle_l}\, H/\nu$ is the local Reynolds number, where $\langle\cdot\rangle_l$ denotes averaging over the cilium region and in time. ($h$, $i$) Normalised Reynolds number $Re(\omega)/Re_{RB}$ and Nusselt number $Nu(\omega)/Nu_{RB}$ vs $\omega/\omega_{c2}$ for different cilium lengths $L$.

critical frequency $\omega_{c2} = Re_l \nu/LH$, and we replot $Re(\omega)/Re_{RB}$ and $Nu(\omega)/Nu_{RB}$ as a function of the normalised frequency $\omega/\omega_{c2}$ for various values of $L$ in figure 3($h$, $i$). The figure demonstrates that both the Reynolds number $Re$ and normalised Nusselt number $Nu$ begin to transition from uplift-driven to vortex-driven heat transfer when $\omega > \omega_{c2}$. This also effectively anticipates the notable reversal in the trend depicted by the final data point in figures 3($h$) and 3($i$).

## 4. Conclusion

In summary, we introduce a novel approach to enhance scalar transport by harnessing the oscillation energy of cilia in chaotic flows, demonstrated via DNS in both two and three dimensions. Our result demonstrates that periodic ciliary oscillations, tuned to specific frequencies, significantly boost scalar transport by overcoming the constraints of laminar boundary layers. The enhanced transport is primarily due to boundary-layer resonance and a transition in the heat transport mode. At medium to low frequencies, the cilia effectively uplift the fluid, improving heat transport through direct vertical displacement. As the frequency increases, the ability of the cilia to induce uplift diminishes, leading to localised vortex formation. This shift is driven by the increasing dominance of the shear



https://doi.org/10.1017/jfm.2025.11000 Published online by Cambridge University Press

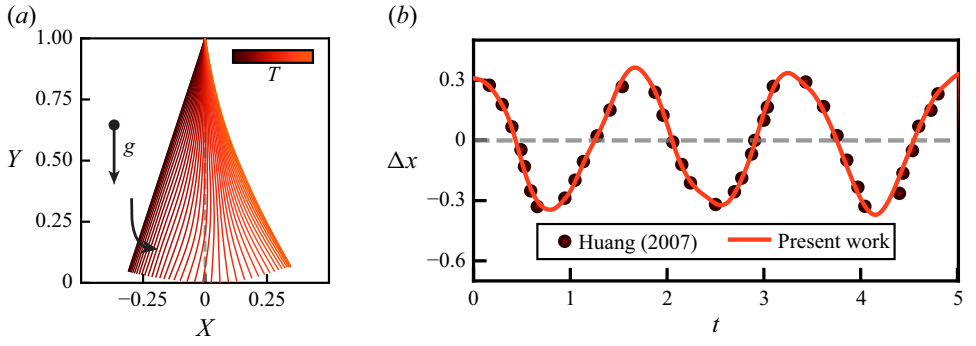



Figure 4. (*a*) Superposition of filament positions at successive times over half an oscillation period. (*b*) Time history of the free end position of the filament, with solid dots taken from Huang *et al.* (2007).

flow dynamics within the ciliary layer. Once the oscillation frequency reaches a critical threshold, the flow intensity becomes strong enough to develop vortices, generated by the unstable shear flow from the rapid directional changes of the oscillating cilia. These vortices significantly improve fluid mixing and heat transport efficiency. Thus, it is the intensified flow within the ciliary layer, driven by high-frequency oscillations, that triggers the transition to a vortex-dominated transfer mechanism. Notably, we employ a symmetric sinusoidal stroke; non-reciprocal strokes should intensify power-phase sweeping, enhance transport and slightly shift the optimal frequency while preserving the boundary-layer sweeping/diffusive scaling. This concept can be similarly applied to other chaotic systems where another force agent drives the chaotic flow rather than buoyancy.

**Supplementary movies.** Supplementary movies are available at https://doi.org/10.1017/jfm.2025.11000.

**Funding.** This work is supported by NSFC Excellence Research Group Program for 'Multiscale Problems in Nonlinear Mechanics' (No.12588201), and it was also supported by the Natural Science Foundation of China under grant nos. 12372219, 52450304, 12432011, 12422208, 12421002, 12372220 and 12502255, the China Postdoctoral Science Foundation under Grant No. 2024M761631 and the New Cornerstone Science Foundation through the New Cornerstone Investigator Program and the XPLORER PRIZE.

**Declaration of interests.** The authors report no conflict of interest.

## Appendix A. Validation of fibre-dynamics numerical solution

We validate our solver by simulating the oscillation of a filament under gravity in a quiescent environment, as described in Huang *et al.* (2007). For finite bending stiffness ($B = 0.01$), the filament oscillates at its natural frequency. As shown in figure 4, our results agree well with Huang *et al.* (2007), using a resolution of 100 Lagrangian points per unit length.

## Appendix B. Critical transition for different parameters

Figure 5 shows $Nu(\omega)/Nu_{RB}$ and $Re(\omega)/Re_{RB}$ versus the normalised frequency $\omega/\omega_c$ for various parameters. At low $\omega$, $Nu(\omega)/Nu_{RB}$ and $Re(\omega)/Re_{RB}$ remain approximately constant, and then increase sharply beyond a critical frequency ($\omega/\omega_c > 1$), supporting the general applicability of our explanation. It is worth noting that the current results were obtained within a limited range, and extending this range could affect the heat transport magnitude. The simulations focus on relatively stiff filaments, and a broader range of $B$ may reveal different behaviours (Zhao *et al.* 2024).



https://doi.org/10.1017/jfm.2025.11000 Published online by Cambridge University Press

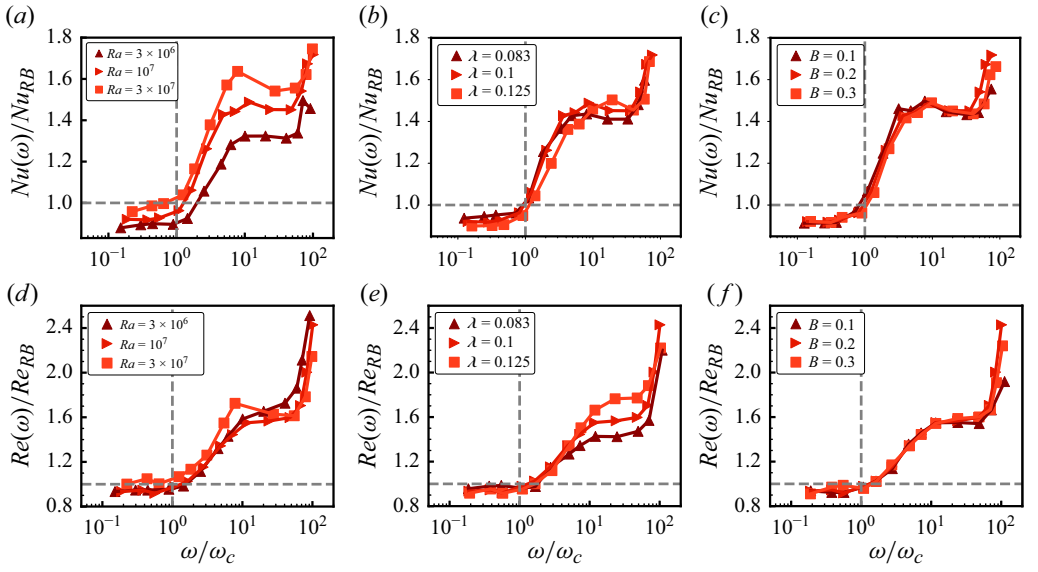



Figure 5. (*a–c*) Normalised Nusselt number $Nu(\omega)/Nu_{RB}$ vs oscillation frequency $\omega/\omega_c$ for various $Ra$ (*a*), spacing $\lambda$ (*b*) and filament rigidity $B$ (*c*). Panels (*d–f*) show $Re/Re_{RB}$ vs $\omega/\omega_c$ for different $Ra$ (*d*), spacing $\lambda$ (*e*) and filament rigidity $B$ (*f*). Here, $Nu_{RB}$ is the Nusselt number for standard RB convection. All data are for two-dimensional simulations.

## References


Ahlers, G., Grossmann, S. & Lohse, D. 2009 Heat transfer and large scale dynamics in turbulent Rayleigh–Bénard convection. *Rev. Mod. Phys.* **81** (2), 503.

Alben, S. 2015 Flag flutter in inviscid channel flow. *Phys. Fluids* **27** (3), 033603.

Banaei, A.A., Rosti, M.E. & Brandt, L. 2020 Numerical study of filament suspensions at finite inertia. *J. Fluid Mech.* **882**, A5.

Bouhouche, K., Valentine, M.S., Le Borgne, P., Lemullois, M., Yano, J., Lodh, S., Nabi, A., Tassin, A.M. & Van Houten, J.L. 2022 Paramecium, a model to study ciliary beating and ciliogenesis: insights from cutting-edge approaches. *Front. Cell Dev. Biol.* **10**, 461.

Brennen, C. & Winet, H. 1977 Fluid mechanics of propulsion by cilia and flagella. *Annu. Rev. Fluid Mech.* **9** (1), 339–398.

Causa, E., Das, D., Feriani, L., Kotar, J. & Cicuta, P. 2025 Cilia dynamics create a dynamic barrier to penetration of the periciliary layer in human airway epithelia. *Proc. Natl Acad. Sci. USA* **122** (28), e2419032122.

Chillà, F. & Schumacher, J. 2012 New perspectives in turbulent Rayleigh–Bénard convection. *Eur. Phys. J. E* **35** (7), 58.

Coq, N., Bricard, A., Delapierre, F.D., Malaquin, L., Du Roure, O., Fermigier, M. & Bartolo, D. 2011 Collective beating of artificial microcilia. *Phys. Rev. Lett.* **107** (1), 014501.

Dong, X., Lum, G.Z., Hu, W., Zhang, R., Ren, Z., Onck, P.R. & Sitti, M. 2020 Bioinspired cilia arrays with programmable nonreciprocal motion and metachronal coordination. *Sci. Adv.* **6** (45), eabc9323.

Elgeti, J. & Gompper, G. 2013 Emergence of metachronal waves in cilia arrays. *Proc. Natl Acad. Sci. USA* **110** (12), 4470–4475.

Eloy, C. & Lauga, E. 2012 Kinematics of the most efficient cilium. *Phys. Rev. Lett.* **109**, 038101.

Esparza López, C. & Lauga, E. 2023 Rate invariance and scallop theorem in viscosity gradients. *Phys. Rev. Fluids* **8**, 063301.

Gaffney, E.A., Gadêlha, H., Smith, D.J., Blake, J.R. & Kirkman Brown, J.C. 2011 Mammalian sperm motility: observation and theory. *Annu. Rev. Fluid Mech.* **43**, 501–528.

Ganedi, L., Oza, A.U., Shelley, M. & Ristroph, L. 2018 Equilibrium shapes and their stability for liquid films in fast flows. *Phys. Rev. Lett.* **121**, 094501.

Gilpin, W., Bull, M.S. & Prakash, M. 2020 The multiscale physics of cilia and flagella. *Nat. Rev. Phys.* **2**, 74–88.

Gu, H., *et al.* 2020 Magnetic cilia carpets with programmable metachronal waves. *Nat. Commun.* **11** (1), 2637.




https://doi.org/10.1017/jfm.2025.11000 Published online by Cambridge University Press

GUO, X.L., WU, J.Z., WANG, B.F., ZHOU, Q. & CHONG, K.L. 2023 Flow structure transition in thermal vibrational convection. *J. Fluid Mech.* **974**, A29.

GUTTAG, M. & REIS, P.M. 2017 Active aerodynamic drag reduction on morphable cylinders. *Phys. Rev. Fluids* **2**, 123903.

HALL, J. & CLARKE, N. 2020 The mechanics of cilium beating: quantifying the relationship between metachronal wavelength and fluid flow rate. *J. Fluid Mech.* **891**, A20.

HUANG, W.X., SHIN, S.J. & SUNG, H.J. 2007 Simulation of flexible filaments in a uniform flow by the immersed boundary method. *J. Comput. Phys.* **226** (2), 2206–2228.

JIANG, H., WANG, D., LIU, S. & SUN, C. 2022 Experimental evidence for the existence of the ultimate regime in rapidly rotating turbulent thermal convection. *Phys. Rev. Lett.* **129**, 204502.

JIANG, H., ZHU, X., WANG, D., HUISMAN, S.G. & SUN, C. 2020 Supergravitational turbulent thermal convection. *Sci. Adv.* **6** (40), eabb8676.

VON KENNE, A., SCHMELTER, S., STARK, H. & BÄR, M. 2025 Synchronization and metachronal waves of elastic cilia caused by unsteady viscous flow. *Phys. Rev. Res.* **7**, L012029.

KIM, M.J., BIRD, J.C., VAN PARYS, A.J., BREUER, K.S. & POWERS, T.R. 2003 A macroscopic scale model of bacterial flagellar bundling. *Proc. Natl Acad. Sci. USA* **100** (26), 15481–15485.

KOBAYASHI, T. & YAMAMOTO, R. 2024 Steady motions of single spherical microswimmers in non-Newtonian fluids. *Phys. Fluids* **36** (12), 121912.

KOYAMA, H., SHI, D. & FUJIMORI, T. 2019 Biophysics in oviduct: planar cell polarity, cilia, epithelial fold and tube morphogenesis, egg dynamics. *Biophys. Physicobiol.* **16**, 89–107.

LAUGA, E. 2011*a* Enhanced diffusion by reciprocal swimming. *Phys. Rev. Lett.* **106**, 178101.

LAUGA, E. 2011*b* Life around the scallop theorem. *Soft Matt.* **7** (7), 3060–3065.

LAUGA, E. & GOLDSTEIN, R.E. 2012 Dance of the microswimmers. *Phys. Today* **65** (9), 30–35.

LEE, T.R., OH, K., CHUNG, J.H., CHANG, Y.S., CHOI, J.B., YAGAWA, G. & KIM, Y.J. 2011 Resonant behavior and microfluidic manipulation of silicone cilia due to an added mass effect. *Soft Matt.* **7** (9), 4325–4334.

LIU, B., POWERS, T.R. & BREUER, K.S. 2011 Force-free swimming of a model helical flagellum in viscoelastic fluids. *Proc. Natl Acad. Sci. USA* **108** (49), 19516–19520.

LIU, J., COSTELLO, J.H. & KANSO, E. 2025*a* Flow physics of nutrient transport drives functional design of ciliates. *Nat. Commun.* **16** (1), 4154.

LIU, J., MAN, Y., COSTELLO, J.H. & KANSO, E. 2025*b* Optimal feeding in swimming and attached ciliates. *J. Fluid Mech.* **1003**, A26.

LOHSE, D. & SHISHKINA, O. 2023 Ultimate turbulent thermal convection. *Phys. Today* **76** (11), 26–32.

LOHSE, D. & SHISHKINA, O. 2024 Ultimate Rayleigh–Bénard turbulence. *Rev. Mod. Phys.* **96**, 035001.

LOHSE, D. & XIA, K.Q. 2010 Small scale properties of turbulent Rayleigh–Bénard convection. *Annu. Rev. Fluid Mech.* **42**, 335–364.

MARCHIOLI, C., ROSTI, M.E. & VERHILLE, G. 2025 Flexible fibers in turbulence. *Annu. Rev. Fluid Mech.* **58**, 167–192.

MATHAI, V., DAS, A., NAYLOR, D.L. & BREUER, K.S. 2023 Shape-morphing dynamics of soft compliant membranes for drag and turbulence modulation. *Phys. Rev. Lett.* **131**, 114003.

MATHAI, V., TZEZANA, G.A., DAS, A. & BREUER, K.S. 2022 Fluid–structure interactions of energy-harvesting membrane hydrofoils. *J. Fluid Mech.* **942**, R4.

MÉDÉRIC, A. & MAHADEVAN, L. 2005 Fluid-flow-induced flutter of a flag. *Proc. Natl Acad. Sci. USA* **102** (6), 1829–1834.

MESDJIAN, O., WANG, C., GSELL, S., D'ORTONA, U., FAVIER, J., VIALLAT, A. & LOISEAU, E. 2022 Longitudinal to transverse metachronal wave transitions in an in vitro model of ciliated bronchial epithelium. *Phys. Rev. Lett.* **129** (3), 038101.

OSTILLA-MONICO, R., YANG, Y.-T., VAN DER POEL, E.P., LOHSE, D. & VERZICCO, R. 2015 A multiple-resolution strategy for direct numerical simulation of scalar turbulence. *J. Comput. Phys.* **301**, 308–321.

PINELLI, A., OMIDYEGANEH, M., BRUCKER, C., REVELL, A., SARKAR, A. & ALINOVI, E. 2017 The PELskin project: part IV—control of bluff body wakes using hairy filaments. *Meccanica* **52** (7), 1503–1514.

VAN DER POEL, E.P., OSTILLA-MÓNICO, R., DONNERS, J. & VERZICCO, R. 2015 A pencil distributed finite difference code for strongly turbulent wall-bounded flows. *Comput. Fluids* **116**, 10–16.

PURCELL, E.M. 1977 Life at low Reynolds number. *Am. J. Phys.* **45** (1), 3–11.

QIU, T., LEE, T.-C., MARK, A.G., MOROZOV, K.I., MÜNSTER, R., MIERKA, O., TUREK, S., LESHANSKY, A.M. & FISCHER, P. 2014 Swimming by reciprocal motion at low Reynolds number. *Nat. Commun.* **5** (1), 5119.

https://doi.org/10.1017/jfm.2025.11000 Published online by Cambridge University Press

SHAPIRO, O.H., FERNANDEZ, V.I., GARREN, M., GUASTO, J.S., DEBAILLON-VESQUE, F.P., KRAMARSKY WINTER, E., VARDI, A. & STOCKER, R. 2014 Vortical ciliary flows actively enhance mass transport in reef corals. *Proc. Natl Acad. Sci. USA* **111** (37), 13391–13396.

SHELLEY, M.J. & ZHANG, J. 2011 Flapping and bending bodies interacting with fluid flows. *Annu. Rev. Fluid Mech.* **43**, 449–465.

SHISHKINA, O. 2021 Rayleigh–Bénard convection: the container shape matters. *Phys. Rev. Fluids* **6** (9), 090502.

SIGGIA, E.D. 1994 High Rayleigh number convection. *Annu. Rev. Fluid Mech.* **26** (1), 137–168.

STEIN, D.B., DE CANIO, G., LAUGA, E., SHELLEY, M.J. & GOLDSTEIN, R.E. 2021 Swirling instability of the microtubule cytoskeleton. *Phys. Rev. Lett.* **126** (2), 028103.

UPFAL, I.M.L., ZHU, Y., HANDY-CARDENAS, E. & BREUER, K. 2025 Shape-morphing membranes augment the performance of oscillating foil energy harvesting turbines. *Phys. Rev. Fluids* **10**, 034702.

VERZICCO, R. & ORLANDI, P. 1996 A finite-difference scheme for three-dimensional incompressible flows in cylindrical coordinates. *J. Comput. Phys.* **123** (2), 402–414.

WANG, B.F., ZHOU, Q. & SUN, C. 2020 Vibration-induced boundary-layer destabilization achieves massive heat transport enhancement. *Sci. Adv.* **6** (21), eaaz8239.

WANG, Z., MATHAI, V. & SUN, C. 2019 Self-sustained biphasic catalytic particle turbulence. *Nat. Commun.* **10** (1), 3333.

XIA, K.Q., CHONG, K.L., DING, G.Y. & ZHANG, L. 2025 Some fundamental issues in buoyancy-driven flows with implications for geophysical and astrophysical systems. *Acta Mech. Sin.* **41** (1), 324287.

XIA, K.Q., HUANG, S.D., XIE, Y.C. & ZHANG, L. 2023 Tuning heat transport via coherent structure manipulation: recent advances in thermal turbulence. *Natl Sci. Rev.* **10** (6), nwad012.

XIA, Y., HU, Z., WEI, D., CHEN, K., PENG, Y. & YANG, M. 2024 Biomimetic synchronization in biciliated robots. *Phys. Rev. Lett.* **133**, 048302.

XU, C., ZHANG, C., BRANDT, L., SONG, J. & SHISHKINA, O. 2025 Direct numerical simulations of turbulent Rayleigh–Bénard convection with polymer additives. *J. Fluid Mech.* **1014**, A22.

ZHAO, H.B., ZHAO, C.B., ZHOU, Q. & CHONG, K.L. 2024 Thermal convection modulated by actively oscillating filament: the effect of filament rigidity. *Intl J. Heat Mass Transfer* **228**, 125649.

ZHU, X., HE, G. & ZHANG, X. 2014 Flow-mediated interactions between two self-propelled flapping filaments in tandem configuration. *Phys. Rev. Lett.* **113** (23), 238105.

https://doi.org/10.1017/jfm.2025.11000 Published online by Cambridge University Press